Journal of Materials Chemistry A

ROYAL SOCIETY OF CHEMISTRY

PAPER

View Article Online
View Journal | View Issue

Cite this: J. Mater. Chem. A, 2021, 9, 8501

A high-throughput study of oxynitride, oxyfluoride and nitrofluoride perovskites†

Hai-Chen Wang, [a] Jonathan Schmidt,[a] Silvana Botti [b] and Miguel A. L. Marques *[a]

Perovskite solar devices are nowadays the fastest advancing photovoltaic technology. Their large-scale application is however restrained by instability and toxicity issues. Alloying is a promising way to stabilize perovskites, optimizing at the same time their absorption and charge-transport properties. We perform an extensive computational study of the thermodynamic stability and electronic properties of oxynitride, oxyfluoride and nitrofluoride perovskites. We consider quaternary stoichiometries of the type ABX_2Y, where A and B are any elements of the periodic table and X and Y are nitrogen, oxygen, or fluorine. As a starting point we explore the composition space using a simple five-atom perovskite unit cell. We then filter the candidate compositions according to their distance to the convex hull of thermodynamic stability. For the most stable systems, we then investigate other prototype structures, including more complex perovskite phases that allow for octahedral distortions, and a few non-perovskite geometries. Furthermore, for some paradigmatic cases, we study the effect of disorder by exhaustive enumeration of all possible disordered stoichiometric phases with up to 20 atoms in the unit cell. Our calculations are in very good agreement with data for experimentally known mixed anionic compounds, and predict a series of novel stable (perovskite and non-perovskite) oxynitride and oxyfluoride phases, including some with unexpected chemical composition, and one single nitrofluoride compound. Finally, we calculate and discuss the electronic properties of these compounds and their potential for application as photovoltaic absorbers.

Received 4th November 2020
Accepted 17th February 2021

DOI: 10.1039/d0ta10781f

rsc.li/materials-a

Introduction

Perovskites are one of the best known and more extensively studied families of compounds. They possess the general formula ABX_3, where X is a halide, a chalcogen, or even nitrogen, and A and B are two cations. Despite numerous applications of perovskites in the most diverse fields of physics and materials science,[1–4] only a restricted number of experimentally accessible ternary systems[5] exist. There are several possibilities to go beyond this limitation, and open the way to new materials with improved properties. For example, one can fill the A sites with organic molecules, leading to organic–inorganic hybrid perovskites such as $CH_3NH_3PbI_3$. Hybrid perovskites have attracted enormous interest in the past few years, in particular due to their application as absorbers in high-efficiency photovoltaic devices.[6–8] This is due to their unique properties, such as their high tolerance to defects,[9] the origin of which is still under debate among sp antibonding coupling,[8] polarons,[10] and lattice softness.[11] Alternatively, one can fill the B site with two different cations, leading to the so-called double perovskites.[12–14] These have, for instance, been proposed as absorbing layers for photovoltaics or as p-type transparent conductive oxides.[15–18] Another possibility to obtain quaternary perovskites, that we address in this article, is to mix more than one anion in the X position, leading to compositions of the type ABX_2Y.[19]

Mixed anion inorganic compounds are a versatile family of materials that contain more than one anionic species in a single phase.[20] The different radii and oxidation states of the two anions offer extra degrees of freedom with respect to the single-anion phase, enabling further control and tuning of electronic properties. In the context of perovskites, the most interesting and also the most studied systems are oxynitride and oxyfluoride compounds.

Several quaternary oxynitrides and oxyfluorides have already been synthesized and characterized in the literature. The most common methods for synthesis are solid-state reactions, low-temperature fluorination or high-pressure synthesis.[21,22] In solid-state reaction methods a mixture of metal oxides and nitrides or fluorides is simply heated in a furnace. One expects that high pressure stabilizes quaternary perovskites, as it suppresses the decomposition to oxides and nitrogen gas, and

[a]Institut für Physik, Martin-Luther-Universität Halle-Wittenberg, 06120 Halle (Saale), Germany. E-mail: miguel.marques@physik.uni-halle.de

[b]Institut für Festkörpertheorie und -Optik, Friedrich-Schiller-Universität Jena, European Theoretical Spectroscopy Facility, Max-Wien-Platz 1, 07743 Jena, Germany

† Electronic supplementary information (ESI) available. See DOI: 10.1039/d0ta10781f

Table 1 Calculated properties for ABN_2O materials. We list the composition, the Goldschmidt tolerance factor t, the τ factor, the energy distance to the convex hull of the simple five-atom cell ($E_{hull}^{(5)}$ in meV per atom), the most stable phase we found (according to the labels defined in Fig. 4), the band gap calculated with the PBE approximation (in eV), the total magnetization of the unit cell per atom (in Bohr magnetons), and the experimental bibliographic reference when available. We only show values of t and τ for materials where the oxidation states of the cations were clearly defined, and for which we had values for the ionic radii. The oxidation states were obtained with PYMATGEN.[41] The values of the band gap in parentheses are experimental results. Note that the PBE approximation underestimates the band gaps, but as we can see from comparison with the experimental numbers the error is systematic. This table includes only the most relevant materials. For more data, please refer to the ESI

Material	t	τ	$E_{hull}^{(5)}$	Str.	E_{hull}	E_{gap}	Mag.	Ref.
$BaReN_2O$	0.99	3.49	125	c	−11	0	0	
$CaReN_2O$	0.87	4.47	146	a	−5	0	0	
$KReN_2O$	1.01	3.71	248	f	7	1.94	0	
$LaNbN_2O$	0.84	3.74	127	a	−32	1.12	0	44
$LaReN_2O$	0.87	2.83	128	a	22	0	0	
$LaTaN_2O$	0.84	3.74	80	a	−45	1.29 (1.9, 2.1)	0	44–49
$LaTcN_2O$	0.86	3.09	170	a	47	0	0	
$NaReN_2O$	0.88	4.09	213	f	46	1.89	0	
$SrReN_2O$	0.93	3.78	81	c	−53	0	0	

allows the reactions to be carried out at higher temperature.[21] Experimentally synthesized compounds are presented in bold in Tables 1–5.

The interest in oxynitride perovskites comes from the numerous possible applications of these compounds. The smaller electronegativity of nitrogen with respect to oxygen leads to band gaps in the visible range, opening the way to a wealth of opto-electronic applications.[23] In fact, and in contrast to oxide perovskites that are usually colourless, these quaternary systems display bright coloring in a diverse color spectrum, enabling their use as, for example, pigments or phosphors[24–26] and photocatalysts.[22,23]

Initially, investigation into oxyfluoride perovskites was motivated by the discovery of superconductivity at 46 K in the cuprate $Sr_2CuO_2F_{2+x}$.[27–29] Oxifluoride systems can also possess interesting magnetic properties. For example, due to the interaction between the Fe^{3+} ions, $BaFeO_2F$, $SrFeO_2F$, and $PbFeO_2F$ exhibit magnetic (antiferromagnetic) ordering until a temperature of around 645 K,[30] 685 K,[31] and >500 K,[32] respectively. Iron-based oxyfluoride perovskites were also shown to exhibit multiferroic behavior.[33]

In this article, we provide a comprehensive computational study of oxynitride, oxyfluoride, and nitrofluoride perovskites. Our objective is threefold: (i) to provide a list of novel compositions that could be likely experimentally synthesized in the perovskite phase; (ii) to provide physical insight into the problem of disorder in these systems; and (iii) to study their electronic properties. We follow a systematic approach to unveil interesting materials that are not simple, evident substitutions of well-studied systems. This is particularly important for nitrofluorides, as no such perovskites are experimentally known at the moment. Our computational tool of choice is density-functional theory (DFT), a quantum approach to calculate the structural and electronic properties of materials which has demonstrated over the years unparalleled accuracy combined with reasonable computational costs.

Clearly, performing a study of the complete chemical space for oxynitride, oxyfluoride, and nitrofluoride perovskites including the effects of distortion, disorder, pressure, temperature, *etc.* is way beyond current computational possibilities. Therefore, we will follow a stepwise procedure conceived to be at the same time predictive and affordable. We start by looking

Table 2 Calculated properties for ABO_2N materials. Legend as in Table 1

Material	t	τ	$E_{hull}^{(5)}$	Str.	E_{hull}	E_{gap}	Mag.	Ref.
$BaNbO_2N$	0.95	3.54	65	a	−22	1.25 (1.8)	0	46 and 47
$BaReO_2N$	0.98	3.47	94	c	−41	0	0	
$BaTaO_2N$	0.95	3.54	33	b	−44	1.43 (1.8)	0	46 and 47
$BaTcO_2N$	0.97	3.48	82	c	−54	0	0	
$CaNbO_2N$	0.83	5.34	193	a	22	1.81 (2.1)	0	46 and 47
$CaReO_2N$	0.86	4.67	164	b	−5	0.41	0	
$CaTaO_2N$	0.83	5.34	146	a	13	1.67 (2.4)	0	46–48 and 50
$CaTcO_2N$	0.85	4.86	176	b	−7	0.44	0	
$KReO_2N$	1.01	3.64	124	b	25	0	0	
$LaHfO_2N$	0.81	5.38	177	a	20	2.53	0	
$LaTaO_2N$	0.83	4.57	220	b	140	0	0	
$LaTiO_2N$	0.86	3.13	121	a	30	1.64 (1.9)	0	44, 49 and 51
$LaZrO_2N$	0.81	5.70	260	a	45	2.53	0	51
$LiReO_2N$	0.78	5.76	223	a	40	0	0	
$NaReO_2N$	0.88	4.09	92	b	−7	0	0	
$PbReO_2N$	0.92	3.80	171	c	34	0	0	
$SrNbO_2N$	0.89	4.07	72	a	−21	1.37 (1.9)	0	46 and 47
$SrReO_2N$	0.92	3.83	87	c	−47	0	0	
$SrTaO_2N$	0.89	4.07	65	b	−14	1.68 (2.1)	0	46–48
$SrTcO_2N$	0.91	3.89	95	c	−47	0	0	

at the simple, five-atom perovskite unit cell. The most interesting systems, from the point of view of thermodynamic stability, are then selected by comparison with the experimental data. We then take into account possible distortions by using more complex prototype structures. Disorder is studied by using exhaustive enumeration methods. Finally, we calculate and discuss the physical properties of some selected compounds.

Methods

We performed DFT calculations using the VASP code,[34,35] where all parameters were set to guarantee compatibility with the data available in the materials project database.[36] We used the PAW[37] datasets of version 5.2 with a cutoff of 520 eV. The Brillouin zone was sampled by Γ-centered *k*-point grids with a uniform density calculated to yield 1000 *k*-points per atom (except where explicitly stated). All forces were converged to better than 0.005 eV $Å^{-1}$. All calculations were performed with spin-polarization using the Perdew–Burke–Ernzerhof[38] (PBE) exchange–correlation functional, with the exception of oxides and fluorides containing Co, Cr, Fe, Mn, Mo, Ni, V, and W, where an on-site Coulomb repulsive interaction U with a value of 3.32, 3.7, 5.3, 3.9, 4,38, 6.2, 3.25, and 6.2 eV, respectively, was added to correct the d-states. Band structures were also calculated with the HSE06 functional.[39]

We prepared all possible compositions of type ABX_2Y, where A and B run over the periodic table up to bismuth (with the exception of the noble gases, including La but removing the other lanthanides), and X and Y are N, O, and F. We used in a first instance the simple five-atom unit cell shown in Fig. 1. Considering the 6 possible combinations of X and Y, this leads to 6 × 3906 different stoichiometries. We optimized the geometry of each one of these structures and calculated their formation energy and used them to build the convex hull of thermodynamic stability using PYMATGEN.[41] This robust open-source Python library for materials analysis is widely used in computational studies for a variety of tasks, including the visualization of calculations and the generation of standardized input files. In our case, we use PYMATGEN to query the materials project database and to calculate the energy distance to the convex hull. The construction of the convex hull considers all possible decomposition channels (in elementary, binary, ternary, and quaternary phases) present in the materials project database,[36] complemented with the compounds found in ref. 42. Specifically, this means that the formation energy of each ABX_2Y perovskite is compared to the formation energy of all stable crystalline phases of the A–B–X–Y phase diagram.

To study the effect of disorder, we systematically constructed supercells using the software included in ATAT.[43] We restricted the unit cells to a maximum of 20 atoms (4 formula units), and explored all possible ways to fill the Wyckoff 3d position with the X and Y atoms that respected the X_2Y stoichiometry. Equivalent unit cells that were mapped by a symmetry operation were automatically discarded by ATAT.

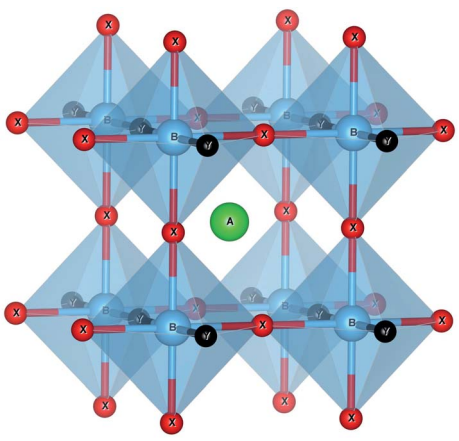

Fig. 1 The crystal structure of the ABX_2Y perovskite used for the high-throughput search. The orange ball denotes the A atom, while cyan balls are B atoms, green balls X atoms and pink balls Y atoms. The unit cell is tetragonal with space group *P*4/*m*2/*m*2/*m* (#123). Image produced with VESTA.[40]

Exploration of the chemical space

It is instructive to analyze the distance to the convex hull of stability (E_{hull}) for all chemical compositions when we use the five-atom perovskite unit cell. A histogram with this information can be found in Fig. 2. Although this plot does not give us information on specific materials, it does give us invaluable insights into the chemistry of inorganic perovskites. Interestingly, the curves for the different anion compositions exhibit different behaviors. For ABO_2N and ABN_2O the histograms are less asymmetric and are centered at around 1.5 eV. There is also a clear difference between ABO_2N and ABN_2O, with the former yielding more stable compounds than the latter. The histograms for the oxyfluorides rise very steeply until around 1 eV and then decay slowly until ∼4 eV. No noticeable difference in stability can be seen for ABO_2F and ABF_2O. The nitrofluorides display very few systems with a small distance to the hull, and show a large difference between ABN_2F and ABF_2N, with the latter yielding considerably more stable structures. The reduced stability of the ABN_2Y crystal phases can be understood by noticing that the −3 standard oxidation state of nitrogen implies that cations A and B together have to compensate for at least a −7 valence. While this is certainly possible, the number of such combinations of A and B is considerably smaller than in the case of anions with lower charge states. Furthermore, the larger difference of ionic radii between N and F (with respect to the N–O and O–F pairs) can also lead to geometrical instabilities, thereby increasing the formation energy of nitrofluoride systems.

The most important information that we can obtain from the distance of the formation energy to the convex hull is which materials are predicted by theory to be stable. It is true that experimentally one can synthesize crystal phases that are not thermodynamically stable (*i.e.*, not on the convex hull of stability), but the difficulty in realizing such phases increases considerably with their energy distance to the hull. We will therefore turn our attention to the materials contained in the left extreme of the distributions in Fig. 2. The selected

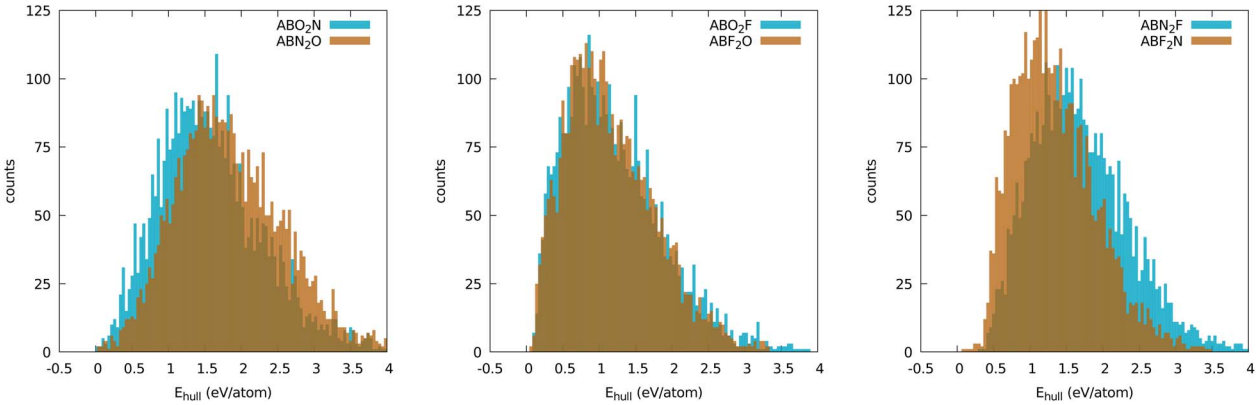

Fig. 2 Distribution of the distances to the convex hull of all oxynitride (left), oxyfluoride (center), and nitrofluoride (right) perovskites. The bins have a size of 40 meV per atom.

compounds are listed, together with information on the experimentally realized phases, in Tables 1–5 and in the ESI.†

Lowest-energy compositions

Before we start discussing our results, we have to define the criteria for filtering in low-energy compositions for further analysis. Typically, this is done by setting a reasonable threshold in the distance to the convex hull. However, several considerations have to be taken into account in our case. First, the five-atom structure we used in the high-throughput search can be further stabilized by distortion (tilting or rotation of the octahedra as common in many perovskites, for example) or by rearranging the atomic positions of the X and Y atoms. As we will see in the following, this can sometimes lead to a decrease of the formation energy of about hundred meV per atom. Then, we can expect a reasonable degree of disorder in the occupation of the X and Y sites, leading to a further decrease of the free energy due to configurational entropy. This term is typically of the order of tens of meV per atom at room temperature.[64] Note that there are still other (de)stabilization mechanisms, such as defects, temperature, pressure, *etc.*, that also lead to corrections to the free-energy. Finally, we should consider the error of the PBE approximation in the estimation of formation energies,[65–68] and hence in the determination of distances to the convex hull. This means that materials with a small positive distance to the hull might still be stable in the experiment.

In order to alleviate these issues, we decided to use a pragmatic approach. We considered our calculations for the few oxynitride and oxyfluoride phases that were synthesized experimentally and observed that all these systems have formation energies close to the convex hull of thermodynamic stability. This fact validates on the one hand our approach to find new materials, and on the other hand it provides us a valid way to set a stability threshold. The experimentally known stable composition with the highest distance to the hull in our five-atom unit cell is $LaZrO_2N$ at 260 meV per atom above the convex hull (although most other experimental compounds lie well below 150 meV per atom). This number is considerably higher than the usual criterion for metastability,[69,70] but one should keep in mind that we are filtering out compounds before having included stabilizing energy contributions coming from octahedral distortions and entropic effects. We will therefore take 260 meV per atom as the maximum distance to the convex hull of stability and pass on for further analysis only compounds that satisfy this condition.

In Tables 1–5 we summarize the most relevant results. The remainder of the data can be found in the ESI.† All structures and a summary of the calculations can be downloaded from our website.‡ At a first glance we find a variety of compositions below the 260 meV per atom stability threshold. The stability of perovskites is often discussed based on the Goldschmidt tolerance factor[71]

$$t = \frac{r_A + r_{anion}}{\sqrt{2}(r_B + r_{anion})}, \quad (1)$$

where r_A, r_B, and r_{anion} are the ionic radii of the A and B cations, and of the anion. More recently,[72] a novel data analytics approach has led to the proposition of a new factor

$$\tau = \frac{r_{anion}}{r_B} n_A \left(n_A - \frac{r_A/r_B}{\log(r_A/r_B)} \right), \quad (2)$$

where n_A is the oxidation state of A. For an experimental dataset of 576 ABX_3 materials, it was found that $0.825 < t < 1.059$ gives a classification accuracy of 74%, while $\tau < 4.18$ has an accuracy of 92%.

To use any of these formulae for mixed anions, we must decide on which value of r_{anion} to use. In line with the suggestion of ref. 72 we decided to use the arithmetic average $r_{anion} = (2r_X + r_Y)/3$. Note that, however, it has been pointed out that the Goldschmidt factor using r_{anion} can fail to capture the stability trends in mixed anionic perovskites[53,73] and pyrochlores.[74] The geometric mean has also been used to approximate the radius of a site with two ions,[75] and more complicated factors that involve, *e.g.*, octahedral factors and atomic packing fractions,

‡ https://tddft.org/bmg/data.php

have also been proposed.[75,76] For simplicity, however, we decided to build our analysis in the traditional t and on τ.

All the considered materials have values of Goldschmidt tolerance factor between 1.09 (for $CsCoF_2O$) and 0.78 (for $LiReO_2N$ and $NaInF_2O$). All in all, this range of [0.78, 1.09] is perfectly consistent with the usual range reported for perovskites.[72] Concerning τ we find that 79% of our low-energy phases have $\tau < 4.18$ and should therefore be stable perovskites according to ref. 72. This percentage of true positives is reasonable, but considerably smaller than the stated accuracy of 92%. In view of this analysis, and considering that it is nowadays possible to perform efficient high-throughput DFT calculations and apply sophisticated machine learning models,[77] it is unclear what is the benefit of using oversimplified empirical models for the prediction of novel stable materials.[78]

One last note concerning materials containing lanthanide atoms: as we removed these elements from our high-throughput search they do not appear in our results. However, one can reasonably expect that materials predicted to be low energy with La are also close to the hull after substitution of La by other lanthanides due to their chemical similarity.[79,80]

Oxynitrides

In what concerns oxynitride compounds of the ABN_2O type, we find 16 systems that satisfy our filtering conditions. Interestingly, they exhibit combinations of cations with diverse oxidation states. For example, I–VII as in $KReN_2O$, II–VI as in $CaReN_2O$, or III–V as in $LaReN_2O$. The lowest of this (at 69 meV per atom above the hull) is $LaTaN_2O$, that has already been experimentally synthesized.[44–49] At the B site, we find mostly a group V (Sr or Ba) or a group VII (Tc or Re) element. Perhaps surprisingly, the chemical element that yields more stable compounds is Re, which can combine with Na, K, Ca, Sr, Ba, La, and Pb. In view of the fact that there are, at the moment, no known Re-based oxynitrides, this finding can open the door to a completely new family of materials. We note that many of these compounds, although having low energy, require cations in less common oxidation states. Therefore, we can probably expect that, if synthesized, they will be off-stoichiometric, either due to the variation in the O–N ratio, or due to the creation of vacancies.

The other stoichiometric oxynitride family, $ABNO_2$, has considerably lower formation energies, so we find many more systems (35) within our energy threshold. In this list, we find cations in the oxidation states I–VI (as in $KReO_2N$), II–V (as in $BaTaO_2N$), and III–IV (as in $LaTiO_2N$). The most likely element that we find at the B-site is again Re, that can be combined with (in ascending order of formation energy) Sr, Na, Ba, K, Ca, Pb, Li, and Rb. Interestingly, this list includes almost all alkali metals, although Li and Rb show clearly decreased stability, but not La, as $LaReNO_2$ appears at 324 meV per atom above the hull. We find a similar situation with Tc at the B-site, yielding stable systems for A = Sr, Ba, Na, Ca, Pb, K, and La. Also many systems with Nb (A = Ba, Sr, Ca, La) and Ta (A = Sr, Ba, Ca, La, Pb, Sn) have small distances to the convex hull. When La is at the B-site, we find stable systems with the A-site being a group IV element (Ti, Zr, or Hf). Finally, we also find systems such as {Sr, Ba}{Mo, Ru}O_2N and {Sr, Ba, Na}OsO_2N.

Oxyfluorides

We now turn our attention to candidate oxyfluoride perovskites. At a glance these systems appear to be considerably more stable than oxynitrides, with 124 compositions of $ABFO_2$ and 134 compositions of ABF_2O below our stability threshold.

For $ABFO_2$ the most common oxidation state of the cations is I–III, although a few rare compounds with II–II (such as $BaMgF_2O$) or III–I (such as $LaLiF_2O$) do appear. The most likely elements occupying the A-site are Sr, Ba or an alkali-metal (in particular K and Rb, and to a lesser extent Na and Cs). The alkali-earths form low-energy oxyfluoride perovskites with a set of mostly first-row metals at the B-site. Particularly interesting are compounds with Mn, Fe, Co, Ni, *etc.* that should lead to materials with magnetic order. When Cs, Rb, and K are found at the A-site, one encounters at the B-site a transition metal. The ones leading to more stable compositions are the heavy elements Bi and Pb or group IV elements (Ti, Zr, or Hf). For Na, on the other hand, the B-site should contain lighter elements such as Ti, V, or Al. We find furthermore several compositions with Pb, Tl, and Ag at the A-site.

The materials that have already been synthesized (see Tables 3 and 4) are consistent with our predictions. We should note, however, that ref. 53 attempted the high pressure synthesis of

Table 3 Calculated properties for ABF_2O materials. Legend as in Table 1

Material	t	τ	$E_{hull}^{(5)}$	Str.	E_{hull}	E_{gap}	Mag.	Ref.
$AgCuF_2O$	0.93	3.75	176	f	33	0	0	
$AgFeF_2O$	0.89	3.85	152	e	64	1.18	1.00	52
$AgGaF_2O$	0.90	3.80	161	f	42	1.16	0	
$BaLiF_2O$			247	d	34	3.38	0	
$CsBiF_2O$	0.90	3.58	120	b	3	2.60	0	
$CsCaF_2O$			218	e	40	3.01	0	
$CsHgF_2O$			176	e	−20	0.55	0.20	
$CsPbF_2O$			64	d	50	1.12	0	
$CsSbF_2O$	1.01	3.23	230	b	30	3.83	0	
$CsSrF_2O$			242	d	44	2.83	0	
$KAgF_2O$	0.92	3.55	198	e	13	0.75	0.20	
$KAlF_2O$	1.02	3.57	218	f	43	4.51	0	
$KAsF_2O$	1.00	3.51	255	e	24	4.32	0	
$KBiF_2O$	0.81	5.00	181	f	−2	3.18	0	
$KSbF_2O$	0.91	3.57	245	b	21	4.19	0	
$NaAlF_2O$	0.89	3.97	190	f	26	4.84	0	
$NaFeF_2O$	0.84	4.33	165	f	44	2.31	1.00	
$NaGaF_2O$	0.85	4.21	202	f	25	3.65	0	
$NaMnF_2O$	0.84	4.33	162	e	44	0.24	0.80	
$RbAgF_2O$	0.97	3.36	189	e	1	0.46	0.20	
$RbAsF_2O$	1.05	3.45	256	a	22	3.55	0	
$RbBiF_2O$	0.85	4.09	133	f	−17	3.24	0	
$RbCuF_2O$	1.07	3.52	170	e	46	0.99	0	
$RbHgF_2O$			167	e	−31	0.89	0.20	
$RbSbF_2O$	0.96	3.36	209	b	17	3.73	0	
$RbTcF_2O$			201	e	−24	0.03	0	
$TlBiF_2O$	0.85	4.19	165	f	21	2.87	0	
$TlGaF_2O$	1.02	3.40	214	f	40	3.24	0	
$TlSbF_2O$	0.95	3.38	222	e	18	3.08	0	
$TlYF_2O$	0.90	3.63	137	f	50	2.39	0	

$NaTiO_2F$, which has essentially the same distance to the hull as $KTiO_2F$, without success (it resulted in a mixture of NaF and TiO_2). This emphasizes that the synthesis of an oxyfluoride material is a complex dynamical process whose success cannot be determined by the simple distance to the convex hull.

Concerning ABF_2O compositions, we could find information on the synthesis of $AgFeF_2O$[52] and of the ternary charge-disproportionate $Tl^{I}Tl^{III}OF_2$ compound.[81] However, our calculations indicate that this family should be at least as common as ABO_2F. For this composition we observe either the I–IV or II–III combination of cations. In particular, we find that the alkalis Cs, Rb, and K can form low-energy compounds with a variety of metals (such as Pb, Bi, Co, Ti, Sc, *etc.*). We also report several materials with Na, but only combined with lighter, first-row cations (Co, Ti, Fe, Al, *etc.*). Finally, there are a series of systems with Ta at the A-site, and with In, Sc, Y, Fe, Co, *etc.* at the B site, and with Ag at the A-site and Fe, Ga, Co, Cu, *etc.* at the B-site.

Nitrofluorides

We also looked into the possibility of obtaining nitrofluoride perovskites. To our knowledge, no such system has been synthesized experimentally. From our results, we can conclude that only one system, specifically $LaMgF_2N$, has chances of being synthesized. The five-atom unit cell is 155 meV per atom above the hull, which is a sizeable but not insurmountable energy distance. All other compositions have an energy distance of more than 300 meV per atom from the hull.

Table 4 Calculated properties for ABO_2F materials. Legend as in Table 1

Material	t	τ	$E_{hull}^{(5)}$	Str.	E_{hull}	E_{gap}	Mag.	Ref.
$AgFeO_2F$	0.81	6.20	269	e	117	0	0.82	
$AgTiO_2F$	0.90	3.81	141	f	26	2.17 (2.8)	0	53
$AgZrO_2F$	0.85	4.14	204	a	69	1.97	0	
$BaAgO_2F$	0.91	3.89	233	f	140	0	0.03	
$BaFeO_2F$	0.95	3.50	130	b	56	1.52	1.00	30 and 54
$BaGaO_2F$	0.97	3.45	248	e	110	3.52	0	
$BaInO_2F$	0.89	4.20	146	b	82	2.05	0	21
$BaMnO_2F$	0.95	3.50	92	b	64	0	0.80	
$BaScO_2F$	0.91	3.86	90	b	13	4.11	0	55
$BaTlO_2F$	0.85	4.98	222	f	75	1.98	0	
$CsTeO_2F$	0.92	3.45	254	a	40	2.41	0	
$KGaO_2F$			255	a	14	1.06	0.10	
$KHfO_2F$	0.93	3.53	141	b	36	4.40	0	
$KNbO_2F$	0.95	3.51	124	c	28	0	0	56
$KTeO_2F$	0.83	4.47	216	e	42	3.01	0	
$KTiO_2F$	0.98	3.52	148	f	11	3.61 (3.2)	0	57 and 58
$KZrO_2F$	0.93	3.54	140	b	38	3.78	0	
$NaNbO_2F$	0.82	4.59	207	a	108	0	0	56
$NaTiO_2F$	0.86	4.18	158	f	31	3.52	0	59
$NaVO_2F$	0.87	4.10	149	f	−2	2.40	0.20	
$PbFeO_2F$	0.90	4.00	195	f	81	2.04	1.00	32 and 60
$PbMnO_2F$	0.90	4.00	155	f	70	0.52	0.80	61
$PbScO_2F$	0.86	4.78	173	f	54	2.82	0.00	62
$RbBiO_2F$			83	c	50	0	0	
$RbIO_2F$			231	a	15	2.07	0	
$RbNbO_2F$	1.00	3.38	144	c	44	0	0	
$RbTeO_2F$	0.87	3.83	182	a	10	2.38	0	
$RbTiO_2F$	1.03	3.44	205	f	2	3.59	0	
$RbVO_2F$	1.05	3.48	229	f	16	2.40	0.20	
$SrCuO_2F$	0.94	3.67	178	e	42	0.84	0	
$SrFeO_2F$	0.89	4.05	171	b	90	1.57	1.00	63
$TlIO_2F$			241	a	15	2.00	0	
$TlTeO_2F$	0.87	3.90	222	a	44	2.64	0	
$TlTiO_2F$	1.03	3.45	228	f	12	3.09	0	

Effects of disorder

Having selected the compositions that possess the smallest formation energies in the perovskite structure, we now investigate how the energy depends on the specific arrangement of the anions. To that end, we pick a few interesting systems (namely $SrTaO_2N$, $LaTaN_2O$, $RbPbF_2O$, $RbBiO_2F$, $KFeF_2O$, $BaVO_2F$, and $LaMgF_2N$) and construct all possible unit-cells with up to 20 atoms by considering the different configurations that we obtain by filling the 3d Wyckoff anionic site with the two different elements. We found 285 non-equivalent structures, for which we performed a further geometry optimization (using 2000 k-points per atom for increased precision). We note that many of these supercells are consistent with the typical deformations present in perovskites, such as tilting or rotation of the octahedra. Therefore, the resulting variations in the formation energy account for contributions coming from the different anion arrangements and the structural deformation upon relaxation.

We found that the different ordering of the anions leads to a spread of energy of 100–150 meV per atom, and to a stabilization that can be as low as 15 meV per atom (for $RbPbF_2O$) to 128 meV per atom (for $LaMgF_2N$) with respect to the five-atom unit cell. We would like to note that these numbers are for the internal energy at $T = 0$ and not for the free energy. Therefore, they do not account for the term that stems from the configurational entropy that further stabilizes disordered phases.

Three examples are shown in Fig. 3, namely $LaTaN_2O$, $SrTaO_2N$, and $RbBiO_2F$. We can see three different behaviors.

In $LaTaN_2O$ the relaxation of the anions leads to a large stabilization (of 124 meV per atom) with respect to the total

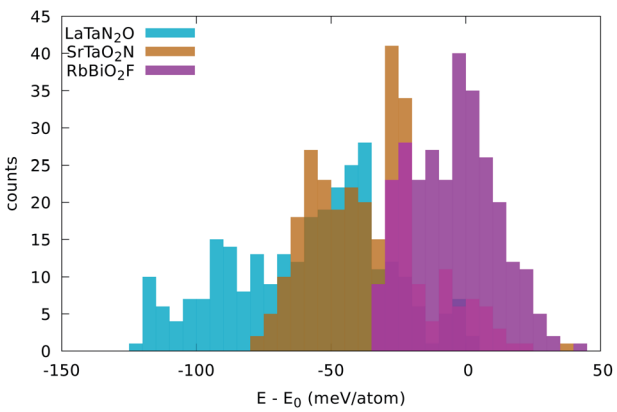

Fig. 3 Distribution of the energy of the disordered cell with respect to the energy of the five-atom unit cell. The width of the bins is 5 meV per atom.

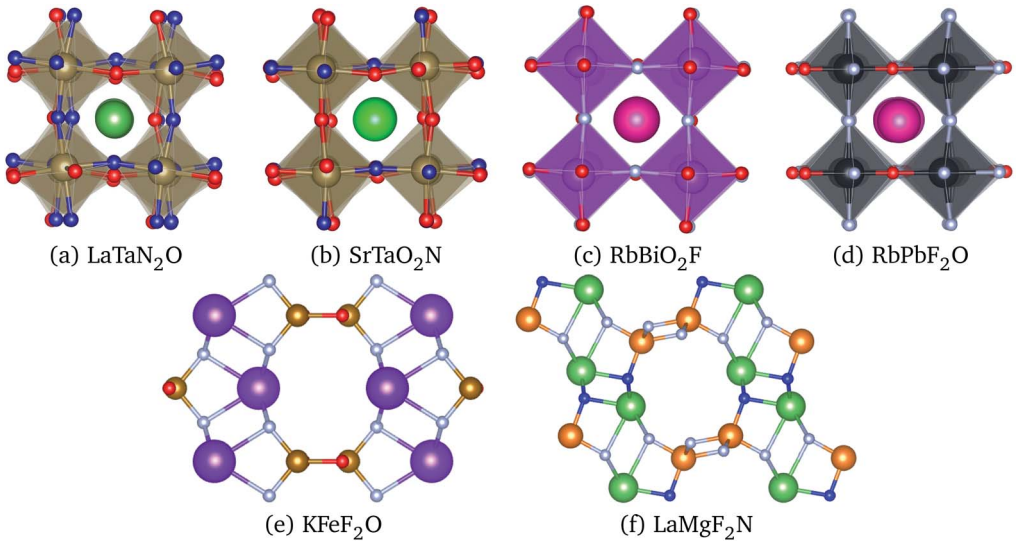

Fig. 4 Crystal structures of the lowest energy phases of (a) $LaTaN_2O$ (space group $P1$, #1), (b) $SrTaO_2N$ (space group $P3_221$, #154), (c) $RbBiO_2F$ (space group $I4/mmm$ #139), (d) $RbPbF_2O$ (space group $Pmma$, #51), (e) $KFeF_2O$ (space group $Cmcm$ #63), and (f) $LaMgF_2N$ (space group $P2_1/m$, #11). K and Bi atoms are in purple, Rb in dark pink, La and Sr in green, Ta in brown, Fe in yellow, Mg in orange, Pb in black, O in red, and F in gray and N in blue. Images produced with VESTA.[40]

energy of the simple five-atom unit cell. The lowest-energy structure we found (shown in Fig. 4) is a low-symmetry 20-atom cell, but we found 13 different anionic arrangements within 10 meV per atom from this phase. In this case the five-atom cell yields the highest energy structure. From the figure we can see the large alternating tilting of the octahedra and the distortions caused by the local mixed-anionic environment. The large distortion can also be assessed from the distributions of the atomic distances that read 3.39–3.69 for La–Ta (the half diagonal of the cube), 2.11–2.30 Å for Ta–O, and 1.92–2.20 Å for the Ta–N distance.

The compound $SrTaO_2N$ is an intermediate case. The relaxation of the anion positions in a larger supercell rearrangement leads to an energy decrease of 79 meV per atom, but we can also find supercells with energy higher by 25 meV per atom than the energy of the five-atom unit-cell. The minimum energy configuration that we found, shown in Fig. 4, has 15 atoms in the unit cell and belongs to the space group $P3_221$ (#154). Interestingly, also the lowest-energy structures of $BaVO_2F$ and $KFeF_2O$ show the same anionic arrangement. In the figure we can observe the tilting of the octahedra, which is however less pronounced than for $LaTaN_2O$. The smaller distortion is also evident from the inspection of the interatomic distances: the Sr–Ta distance is now in the range between 3.47 and 3.59 Å, the Ta–O distance is 2.00–2.15 Å, and the Ta–N distance is 1.98 Å.

Finally, the total energy of $RbBiO_2F$ assumes values essentially centered around the energy of the five-atom cell, with the lowest-energy structure 33 meV per atom below this energy. The most stable phase turns out to be a tetragonal cell with 20 atoms (space group $I4/mmm$ #139). From the small stabilization energy we can expect a small deformation of the lattice, as can be confirmed by visually inspecting Fig. 4. The Rb–Bi bond length ranges between 3.80 and 3.98 Å, the Bi–O distance is in the range 2.14–2.16 Å, and the Bi–F distance is 2.45 Å. In fact, in this structure the F atoms form perfect square motifs.

We observe that in all considered systems except $RbPbF_2O$ the minority anion is never present in opposite vertices of the octahedra, *i.e.* preferring adjacent positions.

Effects of lattice distortion: prototype search

In the previous section we considered nonequivalent configurations due to different occupation of sublattice sites and distortion of the ideal perovskite structure. However, it is certainly possible that some of the considered systems choose to crystallize in other crystallographic arrangements. Ideally, one could use global structural prediction techniques[82] that are capable of predicting the ground-state structure based solely on the chemical composition of the unit cell. Such techniques have already been used, for example, to investigate Cu, Ag, and Au ternary oxides[83] or half-Heusler compounds,[84] or nitride perovskites.[85] However, the large number of systems and the large size of the unit cells required make this approach unaffordable. Therefore, we decided for an alternative procedure that consists in trying out experimental prototype ABX_2Y crystal structures.

To this effect, we searched for stoichiometric compounds (without partial occupancy of the Wyckoff positions) within the Inorganic Crystal Structure Database (ICSD)[86] with compatible chemical compositions. We restricted the search to entries where X and Y are non-metals, but we imposed no further rules to match oxidation states, ionic radii, *etc.* The few systems found are listed in Table 6, and for many of them both X and Y are chalcogens. This again confirms that not so much is experimentally known about mixed anionic systems.

We performed geometry optimization runs for each one of these 20 prototypes, including the two cases ABX_2Y and BAX_2Y, considering again the 7 compositions included earlier in Sec. 4. We observed that several of these prototypes relaxed towards structures already studied in Sec. 4, while others resulted in very high energy phases. A couple of structures, however, turned out to be the ground state for some compositions, namely the crystal structures with ICSD references #68098 and #84635. The structure optimization of the former for $KFeF_2O$ leads to a very different geometry, depicted in Fig. 4, with space group *Cmcm* #63. This structure does not exhibit the traditional octahedral coordination of perovskites, and is 44 meV per atom lower in energy than the $P3_221$ perovskite structure. For $LaMgF_2N$ the ICSD structure #84635 led to the geometry represented in Fig. 4. This phase has the space group $P12_1/m1$ (#11) and is also not a perovskite-like structure. It is only 21 meV per atom more

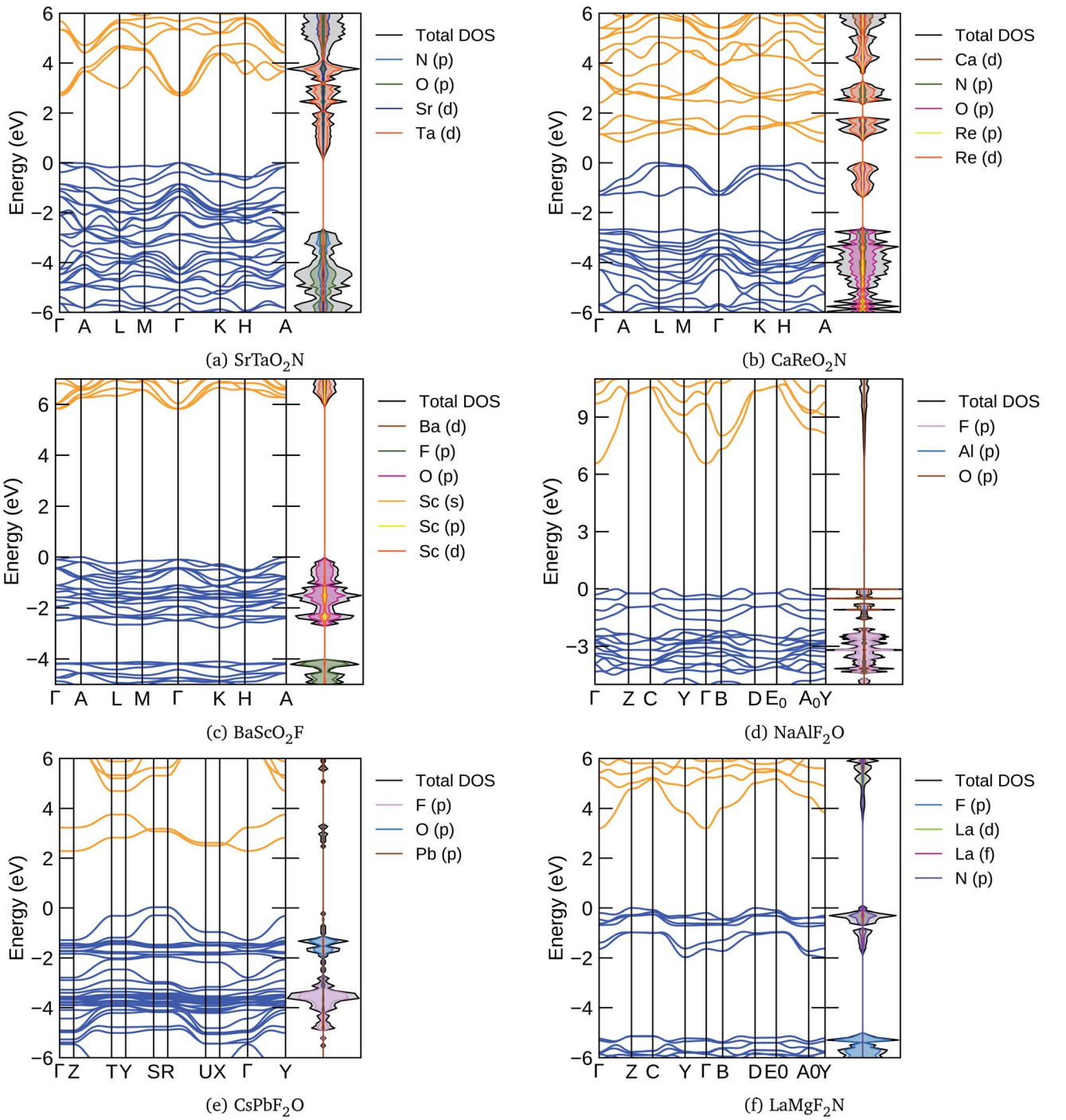

Fig. 5 The band structures and density of electronic states (DOS) of the lowest energy perovskite structures were calculated with the HSE06 functional for (a) $SrTaO_2N$, (b) $CaReO_2N$, (c) $BaScO_2F$, (d) $NaAlF_2O$, (e) $CsPbF_2O$, and (f) $LaMgF_2N$.

stable than the lowest-energy perovskite phase. Interestingly, this structure has clear similarities to the geometry of $KFeF_2O$, as can be seen in the figure.

Having identified the five structures of Fig. 4 as relevant for the low-energy phases of ABX_2Y compounds, we used them for all other compositions within the imposed energy threshold. A plot of the stabilization energy, that we define as the energy of the most stable prototype minus the energy of the five-atom cell, is depicted in Fig. 1. As for the cases discussed above, this energy can vary considerably from essentially zero to 250 meV per atom. We expected to see a correlation between the deviation of the Goldschmidt tolerance factor t from 1 and the stabilization energy. In fact, for values of $t < 0.9$ we expected the perovskite to distort from its cubic form, leading to a considerable decrease of the energy. However, we could only find a very weak correlation in the data, *i.e.* only compounds with very small values of t lowered considerably their energy by distortion. In any case, we should recall that (i) we only used 5 prototypes that clearly do not allow for all possible orthorhombic and rhombohedral distortions that may be favorable for some systems, and (ii) our energies contain two distinct contributions that unfortunately are difficult to disentangle, namely geometrical distortions and effects of disorder.

The most stable structures found for each composition can be found in Tables 1–5. We also present the distance to the convex hull of the lowest energy phase, and its electronic band gap and magnetization (per atom). We should recall that the PBE approximation tends to underestimate the band gaps by nearly a factor of two,[87,88] so real samples will have a gap larger than the one indicated in the table. Comparing with the experimental band gaps indicated in parentheses in the tables, we can see that the error is quite systematic.

Oxynitrides

We want to analyze more in detail the data in Tables 1–5. Most of the experimentally known compounds are on the convex hull of thermodynamic stability, or very close to it. This in our opinion validates the use of the distance to the convex hull as a direct measure of the probability that a certain mixed anionic perovskite can be experimentally realized.

We can also see that most systems seem to indeed crystallize in a perovskite structure, with the exception of $NaReN_2O$, $KReN_2O$, $SrTaN_2O$, $KTcO_2N$, and $SnTaO_2N$. From these non-perovskite systems, the most likely one to be realized in experiments is $KReN_2O$ which appears merely 7 meV per atom above the hull. This is a non-magnetic semiconductor, with a PBE gap of almost 2 eV.

There are a number of systems that appear listed with an ABO_2N composition, but not with an ABN_2O composition (or *vice versa*). These are, for example, the cases of $CaNbO_2N$, $CaTaO_2N$, $CaTcO_2N$, $LaHfO_2N$, $LaReN_2O$, *etc.* Sometimes both compositions appear in Tables 1–5, but one of the variants has a considerably larger distance to the hull compared to the other. Examples are $BaNbO_2N$, $BaTaO_2N$, $LaNbN_2O$, $LaTaN_2O$, *etc.* We see these results as indicating that such systems can be synthesized in the specified stoichiometries, but there is only a limited flexibility for the anion composition range. On the other hand, systems that appear with both compositions should be stable with respect to larger variations of the O/N ratio. These are particularly interesting, as they present the largest potential for the engineering of electronic (or other) properties by adjusting the anionic ratio. The best examples are $CaReO_2N$, $SrReO_2N$, $BaReO_2N$, and $KReO_2N$, although some systems with Tc in the B position or $SrTaO_2N$ are also promising. Note that this last compound is experimentally known[46–48] but not the others in this list.

Finally we notice in the list a few materials with a finite magnetic moment ($BaMoO_2N$, $KTcO_2N$, $SrMoO_2N$, $BaNbN_2O$, $BaTaN_2O$, and $SrNbN_2O$). However, none of these latter is particularly close to the hull, so we will not discuss them in more detail.

In Fig. 5 we present, as an example, the electronic band structure and density of states for $SrTaO_2N$ and $CaReO_2N$. The first crystallizes in the perovskite structure shown in Fig. 4b and presents a rather isotropic band structure with a direct band gap at Γ of 2.70 eV in the HSE06 functional. The lowest conduction bands are highly dispersive, with an effective mass of $m_e^* \sim 0.8\ m_0$. The upper valence bands are much less dispersive, which is reflected in the heavier hole mass of $m_h^* \sim 5\ m_0$. This significant difference between electron and hole masses is present in many of our systems, and has already been discussed in ref. 89. The valence states are mostly composed by p states of N and O with a small contribution coming from Ta d states, while the conduction bands have mainly Ta d character with a small O p character. The reduced hybridization between the anionic p-states and the B-metal states is probably the cause of the heavy holes. Finally, we see very few states associated with Sr in the $[-6, 6]$ eV energy windows, which is compatible with the interpretation that the A atom is fully ionized in the perovskite structure (Fig. 6).

The band structure of $CaReO_2N$ is rather different from that of $SrTaO_2N$, even if they share the same crystal structure. The band gap of 0.87 eV is indirect, with the bottom of the conduction band at A and the top of the valence band along the line connecting H and A. Both electron and hole bands are

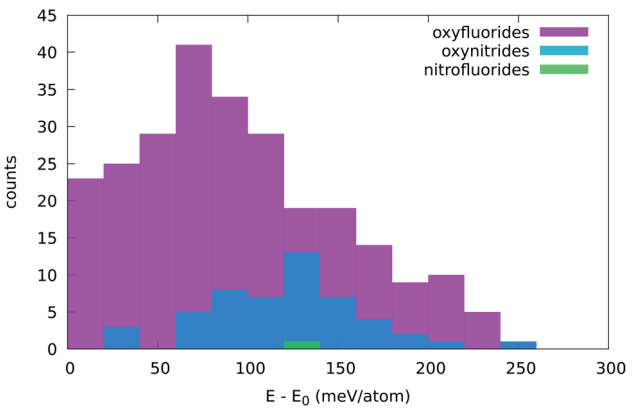

Fig. 6 Distribution of the stabilization energy, defined as the lowest energy of all prototypes used minus the energy of the five-atom cell depicted in Fig. 1. The width of the bins is 20 meV per atom.

mainly composed of Re d states hybridized with p states of O (valence band) or O and N (conduction band). The valence states are split into two manifolds, with the lowest group (starting at around 2.5 eV below the Fermi surface) mostly composed of the anionic p states with a small contribution from Re. The Ca states are found only in the conduction band above 5 eV, again indicating that this atom is ionized in this structure.

Oxyfluorides

From Tables 3 and 4 we can see that there are considerably more oxyfluoride systems, within our formation-energy cutoff, than oxynitrates. However, the lowest energy phases of many of these systems turn out to be a non-perovskite, *i.e.* one of the structures depicted in Fig. 4e and f. Furthermore, some of the experimentally known systems have slightly large distances to the convex hull (>50 meV per atom). Unfortunately, with the available data it is difficult to discern if this is due to the difficulty of describing fluorinated materials with the PBE approximation, or if disorder, defects or alloying have a greater stabilization role in these systems. Furthermore, we note that several of the experimentally known materials are magnetic. It is well known that the vast majority of magnetic semiconductors are indeed anti-ferromagnetic; however, all our calculations are performed for the ferromagnetic phase. This can also lead to an overestimation of the theoretical formation energy of typically a few tens of meV per atom.

With Ag in the A position, we find stable compositions for B = Cu, Fe, Ga, Ti, and Zr. The most stable seems to be $AgTiO_2F$, while $AgZrO_2F$ is the only one that the PBE predicts to crystallize in a perovskite structure. Filling the A site with Ba leads to the stabilization of a series of ABO_2F compositions. Most of these systems have considerable band gaps, with the largest gap of 4.11 eV found for $BaScO_2F$. One band structure of this kind is depicted in Fig. 5c. We can see that the HSE band gap of 5.82 eV between A and Γ is indirect, with the curvature of the conduction bands considerably larger than that of the valence bands. The top of the valence is mainly composed of O p-states with a smaller contribution of Sc states, while the bottom conduction has Sc d-character with a smaller component coming from Ba d and O p levels. The valence bands are split, with the top composed mainly of O p states and the bottom bands exhibiting mainly F p-character. Between the two manifolds there is a gap. These characteristics are shared by many of the oxynitride and nitrofluoride systems, ultimately due to the larger electronegativity of F and of the stronger ionic character of the cation–F bond when compared to the cation–O bond.

Some of the Ba containing materials are magnetic when the B site is occupied by a 3d metal such as Cr, Mn, Fe, or Ni. On the other hand, the only system with a perovskite structure that appears in our list is $BaLiF_2O$, with a rather large PBE band gap of 3.38 eV. As such, we do not expect that the F/O ratio can be considerably increased for Ba-based systems.

Most of the systems in Tables 3 and 4 have an alkali metal in the A position (Na, K, Rb, or Cs). At the B site we find a rather diverse set of metals, ranging from the alkali earths Ca and Sr, passing through the magnetic metals Mn and Fe, a series of transition metals, and even the semi-metal atoms As, Te, and I. Many of these materials retain the perovskite structure, but some relax into the structures of Fig. 4e and f. They are mostly insulators with considerably large band gaps that can reach 4.51 eV for $KAlF_2O$ and 4.84 eV for $NaAlF_2O$. In Fig. 5d we plot the band structure calculated with the HSE06 functional of this latter compound. We can see that the band gap is indirect, and the band structure is anisotropic, as can be expected from the crystal structure depicted in Fig. 4f. We again see a splitting of the valence bands with states with considerable F character in the lower valence band. The effective mass of the electrons is also clearly smaller than that of the holes. Note that the only AB combinations of cations that we can find in both short lists are CsSb and RbBi, so we expect that these systems are particularly resistant to variations of the F/O ratio.

Finally, interestingly, we find in the list the system $CsPbF_2O$ with a perovskite structure at 50 meV per atom above the hull. The counterpart composition, $CsPbO_2F$, appears at 103 meV per atom above the hull, but with the structure of Fig. 4f. The interest in this structure comes from the fact that the perovskite $CsPbI_3$ is the parent inorganic compound[90] for the famous halide perovskites used for photovoltaic applications.[6] Furthermore, the PBE electronic band gap of these systems is quite stable in what regards the composition, going from 1.12 eV for $CsPbF_2O$ to 1.18 eV for $CsPbO_2F$, a value perfectly suitable for absorbers in photovoltaic modules.[91] We should in fact consider that the PBE calculation underestimates the band gap, but we are also neglecting spin–orbit corrections that are sizable for heavy-element compounds and reduce the size of the gap. The HSE band structure of $CsPbF_2O$ is depicted in Fig. 5e. The band gap is indirect, with the top of the valence and bottom of the conduction bands composed of hybridized F p, O p, and Pb states. In this case the separation of the valence into two manifolds is not complete, leading to some overlap between the two sets of bands. The bottom of the conduction band, on the other hand, is separated by more than 1 eV from the rest of the conduction band.

Nitrofluorides

The calculated properties for $LaMgF_2N$ are shown in Table 5. We can see that this system is considerably stabilized by relaxing into the structure of Fig. 4f, which lies just 19 meV per atom above the hull. This is a large band gap semiconductor, with a PBE band gap of 2.26 eV. The HSE band structure of this material is presented in Fig. 5f. The highly dispersive lowest conduction band is mainly constructed from La d states, while the top valence has mostly N p character with smaller La d character. In the case of this nitrofluoride system we also see a clear splitting of the valence bands. However, due to the

Table 5 Calculated properties for ABF_2N materials. Legend as in Table 1

Material	t	τ	$E_{hull}^{(5)}$	Str.	E_{hull}	E_{gap}	Mag.	Ref.
$LaMgF_2N$	0.81	5.64	155	f	19	2.26	0	

Table 6 Entries with composition $ABXY_2$ and without partial occupancy of the Wyckoff positions found in the ICSD where X and Y are non-metals. We present the ICSD number, the chemical composition, the space group, and the number of atoms in the primitive unit cell

ICSD #	Composition	Spg.	N_{atoms}
80	$CeBiOS_2$	*P*4/*nmm* (#129)	10
2238	$LaGaOS_2$	*Pmca* (#57)	20
14 191	$CeCrOS_2$	*B*112/*m* (#12)	10
14 192	$LaCrOS_2$	*Pbnm* (#62)	20
38 636	$NaNbO_2F$	*Pbnm* (# 62)	20
48 024	$GaLaOSe_2$	$P2_1ab$ (#29)	20
54 075	$CeCrOSe_2$	*B*112/*m* (#12)	10
66 246	$AsPbO_2Cl$	$P2_12_12_1$ (#19)	40
68 098	$PtCOI_2$	*C*12/*c*1 (#15)	20
69 869	$CaFeO_2Cl$	*A*1*m*1 (#8)	10
84 635	$CaBiO_2Cl$	$P12_1/m1$ (#11)	10
86 229	$PbSbO_2Cl$	*Cmcm* (#63)	10
171 722	$CdSbS_2Cl$	*Pnma* (#62)	20
171 723	$CdSbS_2Br$	*C*12/*m*1 (#12)	10
244 028	$LaVSe_2O$	*C*12/*m*1 (#12)	10
411 137	$TaSrNO_2$	*I*4/*mcm* (#140)	10
411 138	$TaLaN_2O$	*C*12/*m*1 (#12)	10
413 289	$CuBiSCl_2$	*Cmcm* (#63)	10
419 916	$LaFCN_2$	*Cmcm* (#63)	10
424 505	$NaBOF_2$	*C*12/*c*1 (#15)	30

strongest electronegativity difference of N and F, the gap between the two manifolds is considerably larger than for the oxyfluoride systems.

Although $LaMgF_2N$ is the only nitrofluoride system that we predict to have possibilities to be realized experimentally, we recall that La is often easily substituted by other lanthanides (or actinides),[80] giving us hope that such nitrofluoride systems can be discovered in the future.

Conclusions

From our extensive computational study of quaternary oxynitride, oxyfluoride, and nitrofluoride perovskites it is clear that there are many more compounds that are experimentally accessible than the few systems that have been discovered to date. Some of them can be obtained by simple chemical substitutions of known compounds, such as $LaHfO_2N$ or $AgTiO_2F$ that can be obtained by substituting Zr in $LaZrO_2N$ or in $AgZrO_2F$. However, many of the predicted materials do not have an experimentally known counterpart, such as the many Re-based oxynitride systems that we found. We note that although many of the low-energy compositions seem to crystallize in a perovskite phase, some systems prefer other atomic arrangements that do not exhibit the famous octahedra. Furthermore, we show that changing the arrangement of the anions and allowing for geometrical distortions can stabilize the structure of the perovskites by up to 150 meV per atom, although this number is highly dependent on the composition. This stabilization is in many cases fundamental, as it makes the composition thermodynamically stable, even without the need to resort to entropic arguments.

Many of our systems turn out to be semiconducting or insulating, with electronic band gaps going from a fraction of an eV to several eV. Often the electron bands are highly dispersive, leading to rather small electron effective masses, while the hole bands are considerably flatter. This can be understood from the reduced hybridization between the cationic states and the anionic p levels. Furthermore, for the fluorine compounds we find that the valence states are often split, with the top of the valence characterized by a strong p-character from O or N atoms, and the lower manifold of states stemming from the F states. The splitting is considerably larger for the nitrofluoride systems than for the oxifluorides indicating that this is due to the larger electronegativity of F leading to a cation–F bond with a stronger ionic character. However, and in spite of these common features, we find a multitude of behaviors that illustrate the diversity and importance of these mixed ionic systems.

Our results confirm that alloying on the anion sublattice is a promising strategy to improve the stability and engineer the band gap of perovskite absorbers.

Conflicts of interest

There are no conflicts to declare.

Acknowledgements

S. B. and M. A. L. M. acknowledge financial support from the DFG through Projects MA 6787/1-1 and BO 4280/8.

Notes and references

1 M. Liu, M. B. Johnston and H. J. Snaith, *Nature*, 2013, **501**, 395–398.
2 S. D. Stranks and H. J. Snaith, *Nat. Nanotechnol.*, 2015, **10**, 391–402.
3 G. Schileo and G. Grancini, *JPhys Energy*, 2020, **2**, 021005.
4 D. W. deQuilettes, K. Frohna, D. Emin, T. Kirchartz, V. Bulovic, D. S. Ginger and S. D. Stranks, *Chem. Rev.*, 2019, **119**, 11007–11019.
5 J. Schmidt, J. Shi, P. Borlido, L. Chen, S. Botti and M. A. L. Marques, *Chem. Mater.*, 2017, **29**, 5090–5103.
6 P. K. Nayak, S. Mahesh, H. J. Snaith and D. Cahen, *Nat. Rev. Mater.*, 2019, **4**, 269–285.
7 A. K. Jena, A. Kulkarni and T. Miyasaka, *Chem. Rev.*, 2019, **119**, 3036–3103.
8 W.-J. Yin, J.-H. Yang, J. Kang, Y. Yan and S.-H. Wei, *J. Mater. Chem. A*, 2015, **3**, 8926–8942.
9 W.-J. Yin, T. Shi and Y. Yan, *Appl. Phys. Lett.*, 2014, **104**, 063903.
10 K. Miyata, T. L. Atallah and X.-Y. Zhu, *Sci. Adv.*, 2017, **3**, e1701469.
11 W. Chu, Q. Zheng, O. V. Prezhdo, J. Zhao and W. A. Saidi, *Sci. Adv.*, 2020, **6**, eaaw7453.
12 M. Anderson, K. Greenwood, G. Taylor and k. Poepellmeier, *Prog. Solid State Chem.*, 1993, **22**, 197–233.

13 A. Hossain, P. Bandyopadhyay and S. Roy, *J. Alloys Compd.*, 2018, **740**, 414–427.
14 E. Meyer, D. Mutukwa, N. Zingwe and R. Taziwa, *Metals*, 2018, **8**, 667.
15 E. Greul, M. L. Petrus, A. Binek, P. Docampo and T. Bein, *J. Mater. Chem. A*, 2017, **5**, 19972–19981.
16 J. Kangsabanik, V. Sugathan, A. Yadav, A. Yella and A. Alam, *Phys. Rev. Mater.*, 2018, **2**, 055401.
17 E. T. McClure, M. R. Ball, W. Windl and P. M. Woodward, *Chem. Mater.*, 2016, **28**, 1348–1354.
18 H.-C. Wang, P. Pistor, M. A. Marques and S. Botti, *J. Mater. Chem. A*, 2019, **7**, 14705–14711.
19 Y. Kobayashi, Y. Tsujimoto and H. Kageyama, *Annu. Rev. Mater. Res.*, 2018, **48**, 303–326.
20 H. Kageyama, K. Hayashi, K. Maeda, J. P. Attfield, Z. Hiroi, J. M. Rondinelli and K. R. Poeppelmeier, *Nat. Commun.*, 2018, **9**, 772.
21 T. Katsumata, R. Suzuki, N. Satoh, S. Suzuki, M. Nakashima, Y. Inaguma, D. Mori, A. Aimi and Y. Yoneda, *J. Solid State Chem.*, 2019, **279**, 120919.
22 M. Ahmed and G. Xinxin, *Inorg. Chem. Front.*, 2016, **3**, 578–590.
23 M. Sakar, R. M. Prakash, K. Shinde and G. R. Balakrishna, *Inorg. Chem. Front.*, 2020, **45**, 7691–7705.
24 R.-J. Xie and H. T. B. Hintzen, *J. Am. Ceram. Soc.*, 2013, **96**, 665–687.
25 R. Aguiar, D. Logvinovich, A. Weidenkaff, A. Rachel, A. Reller and S. G. Ebbinghaus, *Dyes Pigm.*, 2008, **76**, 70–75.
26 R.-J. Xie and N. Hirosaki, *J. Adv. Mater.*, 2007, **8**, 588–600.
27 M. G. Francesconi and C. Greaves, *Supercond. Sci. Technol.*, 1997, **10**, A29–A37.
28 C. Greaves and M. G. Francesconi, *Curr. Opin. Solid State Mater. Sci.*, 1998, **3**, 132–136.
29 E. E. McCabe and C. Greaves, *J. Fluorine Chem.*, 2007, **128**, 448–458.
30 R. Heap, P. R. Slater, F. J. Berry, O. Helgason and A. J. Wright, *Solid State Commun.*, 2007, **141**, 467–470.
31 F. J. Berry, R. Heap, O. Helgason, E. A. Moore, S. Shim, P. R. Slater and M. F. Thomas, *J. Condens. Matter Phys.*, 2008, **20**, 215207.
32 Y. Inaguma, J.-M. Greneche, M.-P. Crosnier-Lopez, T. Katsumata, Y. Calage and J.-L. Fourquet, *Chem. Mater.*, 2005, **17**, 1386–1390.
33 S. T. Hartman, S. B. Cho and R. Mishra, *Inorg. Chem.*, 2018, **57**, 10616–10624.
34 G. Kresse and J. Furthmüller, *Phys. Rev. B: Condens. Matter Mater. Phys.*, 1996, **54**, 11169–11186.
35 G. Kresse and J. Furthmüller, *Phys. Rev. B: Condens. Matter Mater. Phys.*, 1996, **54**, 11169–11186.
36 A. Jain, S. P. Ong, G. Hautier, W. Chen, W. D. Richards, S. Dacek, S. Cholia, D. Gunter, D. Skinner, G. Ceder and K. a. Persson, *APL Mater.*, 2013, **1**, 011002.
37 P. E. Blöchl, *Phys. Rev. B: Condens. Matter Mater. Phys.*, 1994, **50**, 17953–17979.
38 J. P. Perdew, K. Burke and M. Ernzerhof, *Phys. Rev. Lett.*, 1996, **77**, 3865–3868.
39 A. V. Krukau, O. A. Vydrov, A. F. Izmaylov and G. E. Scuseria, *J. Chem. Phys.*, 2006, **125**, 224106.
40 K. Momma and F. Izumi, *J. Appl. Crystallogr.*, 2011, **44**, 1272–1276.
41 S. P. Ong, W. D. Richards, A. Jain, G. Hautier, M. Kocher, S. Cholia, D. Gunter, V. L. Chevrier, K. A. Persson and G. Ceder, *Comput. Mater. Sci.*, 2013, **68**, 314–319.
42 H.-C. Wang, S. Botti and M. Marques, *npj Comput. Mater.*, 2020.
43 A. van de Walle, *Calphad*, 2009, **33**, 266–278.
44 R. Marchand, F. Pors and Y. Laurent, *Ann. Chim.*, 1991, 553–560.
45 M. Liu, W. You, Z. Lei, T. Takata, K. Domen and C. Li, *Chin. J. Catal.*, 2006, **27**, 556–558.
46 Y.-I. Kim, P. M. Woodward, K. Z. Baba-Kishi and C. W. Tai, *Chem. Mater.*, 2004, **16**, 1267–1276.
47 F. Oehler and S. G. Ebbinghaus, *Solid State Sci.*, 2016, **54**, 43–48.
48 E. Günther, R. Hagenmayer and M. Jansen, *Z. Anorg. Allg. Chem.*, 2000, **626**, 1519–1525.
49 Y.-I. Kim, PhD thesis, The Ohio State University, 2005.
50 R. Marchand, F. Pors and Y. Laurant, *Rev. Int. Hautes Temp. Refract.*, 1986, **23**, 11–15.
51 S. J. Clarke, B. P. Guinot, C. W. Michie, M. J. C. Calmont and M. J. Rosseinsky, *Chem. Mater.*, 2002, **14**, 288–294.
52 F. Takeiri, T. Yamamoto, N. Hayashi, S. Hosokawa, K. Arai, J. Kikkawa, K. Ikeda, T. Honda, T. Otomo, C. Tassel, K. Kimoto and H. Kageyama, *Inorg. Chem.*, 2018, **57**, 6686–6691.
53 Y. Inaguma, K. Sugimoto and K. Ueda, *Dalton Trans.*, 2020, **49**, 6957–6963.
54 F. J. Berry, F. C. Coomer, C. Hancock, Ö. Helgason, E. A. Moore, P. R. Slater, A. J. Wright and M. F. Thomas, *J. Solid State Chem.*, 2011, **184**, 1361–1366.
55 R. Needs and M. Weller, *J. Solid State Chem.*, 1998, **139**, 422–423.
56 W. Rüdorff and D. Krug, *Z. Anorg. Allg. Chem.*, 1964, **329**, 211–217.
57 B. Chamberland, *Mater. Res. Bull.*, 1971, **6**, 311–315.
58 T. Katsumata, H. Umemoto, Y. Inaguma, D. Fu and M. Itoh, *J. Appl. Phys.*, 2008, **104**, 044101.
59 V. Zaitsev and V. Senin, *Vestn. Otd. nauk Zemle*, 2012, **4**, 8.
60 T. Katsumata, A. Takase, M. Yoshida, Y. Inaguma, J. E. Greedan, J. Barbier, L. M. D. Cranswick and M. Bieringer, *MRS Online Proc. Libr.*, 2006, **988**, 0988-QQ06-03.
61 T. Katsumata, M. Nakashima, Y. Inaguma and T. Tsurui, *Bull. Chem. Soc. Jpn.*, 2012, **85**, 397–399.
62 T. Katsumata, M. Nakashima, H. Umemoto and Y. Inaguma, *J. Solid State Chem.*, 2008, **181**, 2737–2740.
63 F. J. Berry, X. Ren, R. Heap, P. Slater and M. F. Thomas, *Solid State Commun.*, 2005, **134**, 621–624.
64 F. Brivio, C. Caetano and A. Walsh, *J. Phys. Chem. Lett.*, 2016, **7**, 1083–1087.
65 R. Sarmiento-Pérez, S. Botti and M. A. L. Marques, *J. Chem.*, 2015, **11**, 3844–3850.

66 F. Tran, J. Stelzl and P. Blaha, *J. Chem. Phys.*, 2016, **144**, 204120.
67 V. Stevanović, S. Lany, X. Zhang and A. Zunger, *Phys. Rev. B: Condens. Matter Mater. Phys.*, 2012, **85**, 115104.
68 Y. Zhang, D. A. Kitchaev, J. Yang, T. Chen, S. T. Dacek, R. A. Sarmiento-Pérez, M. A. L. Marques, H. Peng, G. Ceder, J. P. Perdew and J. Sun, *npj Comput. Mater.*, 2018, **4**, 9.
69 W. Sun, S. T. Dacek, S. P. Ong, G. Hautier, A. Jain, W. D. Richards, A. C. Gamst, K. A. Persson and G. Ceder, *Sci. Adv.*, 2016, **2**, e1600225.
70 A. A. Emery and C. Wolverton, *Sci. Data*, 2017, **4**, 170153.
71 V. M. Goldschmidt, *Sci. Nat.*, 1926, **14**, 477–485.
72 C. J. Bartel, C. Sutton, B. R. Goldsmith, R. Ouyang, C. B. Musgrave, L. M. Ghiringhelli and M. Scheffler, *Sci. Adv.*, 2019, **5**, eaav0693.
73 G. Pilania, A. Ghosh, S. T. Hartman, R. Mishra, C. R. Stanek and B. P. Uberuaga, *npj Comput. Mater.*, 2020, **6**, 71.
74 R. Mouta, R. X. Silva and C. W. A. Paschoal, *Acta Crystallogr., Sect. B: Struct. Sci.*, 2013, **69**, 439–445.
75 W. Li, E. Ionescu, R. Riedel and A. Gurlo, *J. Mater. Chem. A*, 2013, **1**, 12239.
76 Q. Sun and W.-J. Yin, *J. Am. Chem. Soc.*, 2017, **139**, 14905–14908.
77 J. Schmidt, M. R. G. Marques, S. Botti and M. A. L. Marques, *npj Comput. Mater.*, 2019, **5**, 83.
78 J. George, D. Waroquiers, D. Di Stefano, G. Petretto, G.-M. Rignanese and G. Hautier, *Angew. Chem., Int. Ed.*, 2020, **59**, 7569–7575.
79 H. Glawe, A. Sanna, E. K. U. Gross and M. A. L. Marques, *New J. Phys.*, 2016, **18**, 093011.
80 J. A. Flores-Livas, R. Sarmiento-Pérez, S. Botti, S. Goedecker and M. A. Marques, *J. Phys. Mater.*, 2019, **2**, 025003.
81 G. Demazeau, I. Grannec, A. Marbeuf, J. Portier and P. Hagenmuller, *C. R. Acad. Sci.*, 1969, **269**, 987–988.
82 A. R. Oganov, *Modern Methods of Crystal Structure Prediction*, John Wiley & Sons, 2011.
83 T. F. T. Cerqueira, S. Lin, M. Amsler, S. Goedecker, S. Botti and M. A. L. Marques, *Chem. Mater.*, 2015, **27**, 4562–4573.
84 F. Yan, X. Zhang, Y. G. Yu, L. Yu, A. Nagaraja, T. O. Mason and A. Zunger, *Nat. Commun.*, 2015, **6**, 7308.
85 R. Sarmiento-Perez, T. F. Cerqueira, S. Körbel, S. Botti and M. A. Marques, *Chem. Mater.*, 2015, **27**, 5957–5963.
86 *Crystallographic Databases*, ed. G. G. F. H. Allen and R. Sievers, International Union of Crystallography, Chester, 1987.
87 P. Borlido, T. Aull, A. W. Huran, F. Tran, M. A. L. Marques and S. Botti, *J. Chem.*, 2019, **15**, 5069–5079.
88 P. Borlido, J. Schmidt, A. W. Huran, F. Tran, M. A. L. Marques and S. Botti, *npj Comput. Mater.*, 2020, **6**, 96.
89 I. E. Castelli, D. D. Landis, K. S. Thygesen, S. Dahl, I. Chorkendorff, T. F. Jaramillo and K. W. Jacobsen, *Energy Environ. Sci.*, 2012, **5**, 9034–9043.
90 W. Xiang and W. Tress, *J. Adv. Mater.*, 2019, **31**, 1902851.
91 W. Shockley and H. J. Queisser, *J. Appl. Phys.*, 1961, **32**, 510–519.